


RESEARCH ARTICLE | NOVEMBER 01 2022

Numerical study on wave configuration of wedge-induced oblique detonation wave: Reactive boundary layer effect

Li Yang (杨理); Lianjie Yue (岳连捷) ; Dehai Yu (于德海); ... et. al

 Check for updates

Physics of Fluids 34, 116103 (2022)

<https://doi.org/10.1063/5.0118194>



View
Online



Export
Citation

CrossMark

Articles You May Be Interested In

Numerical investigation of free oblique detonation wave induced by non-intrusive energy deposition

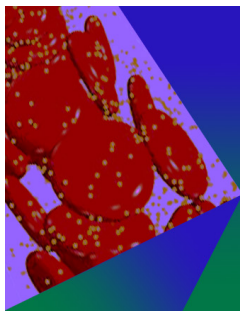
AIP Advances (December 2021)

Characteristics of reattached oblique detonation induced by a double wedge

Physics of Fluids (March 2023)

Structure of wedge-induced oblique detonation in acetylene-oxygen-argon mixtures

Physics of Fluids (February 2019)



Physics of Fluids

Special Topic: Flow and Forensics

Submit Today!

 AIP
Publishing

 AIP
Publishing

Numerical study on wave configuration of wedge-induced oblique detonation wave: Reactive boundary layer effect

Cite as: Phys. Fluids **34**, 116103 (2022); doi: 10.1063/5.0118194

Submitted: 4 August 2022 · Accepted: 5 October 2022 ·

Published Online: 1 November 2022



View Online



Export Citation



CrossMark

Li Yang (杨理),^{1,2}  Lianjie Yue (岳连捷),^{1,3,a)}  Dehai Yu (于德海),⁴  and Zheng Chen (陈正)⁴ 

AFFILIATIONS

¹State Key Laboratory of High Temperature Gas Dynamics, Institute of Mechanics, Chinese Academy of Sciences, Beijing 100190, China

²School of Aeronautics, Chongqing Jiaotong University, Chongqing 402247, China

³School of Engineering Sciences, University of Chinese Academy of Sciences, Beijing 100049, China

⁴State Key Laboratory for Turbulence and Complex Systems (SKLTCS), Center for Applied Physics and Technology (CAPT), Department of Mechanics and Engineering Science, College of Engineering, Peking University, Beijing 100871, China

^{a)} Author to whom correspondence should be addressed: yuelj@imech.ac.cn

ABSTRACT

A numerical simulation solving the Reynolds-averaged Navier–Stokes equation is presented to investigate the initiation and evolution of the wedge-induced oblique detonation wave (ODW) with emphasis on the effects of the burning boundary layer. The nondimensional activation energy (E_a) is selected as the bifurcate parameter, which varies from 30 to 50. The largest induction ignition length behind the oblique shock/detonation wave is shown to be proportional to the E_a . The initiation of ODW can be attributed to the collision and diffraction of reactive waves. The wave configuration, a series of compression waves (or shock wave), is observed at the conjunction point of the burning boundary layer and combustion wave, which intensifies the pressure jump as increasing the E_a . The polar line analysis demonstrates that the pressure jump triggers the transition from regular reflection to Mach reflection near triple-point. The oscillations of the ODW wave structures, for example, the triple-point and Mach stem, can be attributed to the Rayleigh–Taylor instabilities developed on the reaction front of the boundary layer, which shall be appropriately suppressed to remain the steadiness of the ODW and flow configuration.

Published under an exclusive license by AIP Publishing. <https://doi.org/10.1063/5.0118194>

I. INTRODUCTION

Detonation has attracted increasing attention in advanced air-breathing propulsion systems aiming at hypersonic flight because of superior thermodynamic cycle efficiency compared with the conventional constant-pressure combustion.^{1,2} A variety of detonation-based propulsion schemes have been proposed and tested,^{3,4} in which the oblique detonation wave engines (ODWEs) have stimulated researchers' interest because of their promising suitability in practical applications.⁵ Figure 1 shows the schematic of a typical ODWE, in which an oblique detonation wave (ODW) is established on the wedge of the combustor.⁶ ODWEs can also be interpreted as shock-induced combustion ramjet (shcramjet),⁷ which has the advantages of compact engine structure and decent thrust performance due to pressure-gain combustion. Jiang *et al.*⁸ produced a standing ODW with 50 ms time at $Ma = 9$ inflow condition through a ground test conducted in a

hypersonic flight-duplicate shock tunnel, which suggested that ODWE could operate under hypersonic flow conditions.

Figure 1 shows the typical wave configuration of delayed ODW, in which the triple-point connects an inert oblique shock wave (OSW) emanated from wedge tip, a combustion wave (CW) developed from wedge surface, and an oblique detonation front.⁹ Such flow structure was observed in a number of experimental investigations^{8,10–13} and has been the spot of various numerical studies.^{14–18} The essential behaviors of ODW, such as OSW-to-ODW transition pattern,¹⁹ cellular-like structures, and ODW evolution, have been widely investigated by mean of numerical simulation solving Euler equation; that is, the viscous effect of fluid motion is excluded. To categorize the transition patterns, various factors have been tested in previous studies, including the critical Mach number,²⁰ the ratio of the induction time to the total reaction time,¹⁵ dilution ratio of argon,²¹ and the ratio of

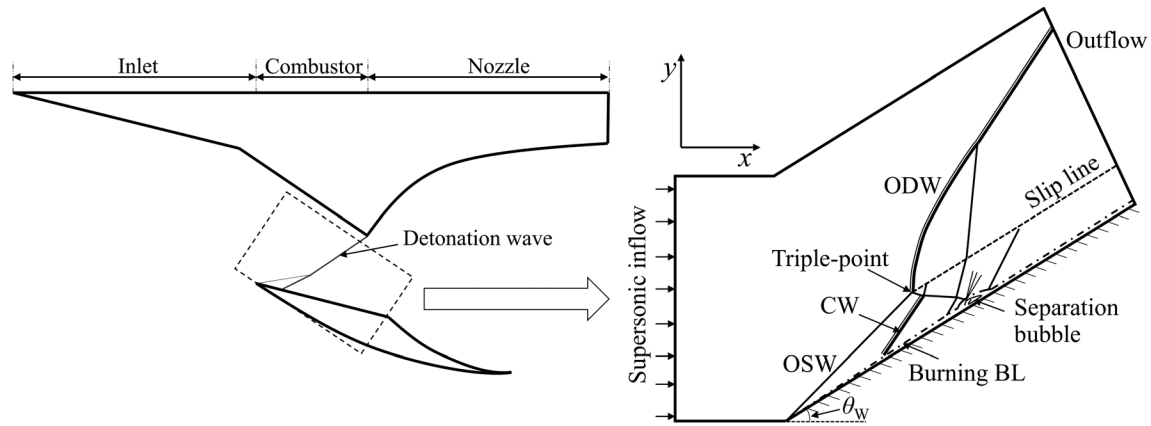


FIG. 1. Schematic depiction of oblique detonation wave engine (left) and its classic flow field (right).

the inflow velocity to Chapman–Jouguet (CJ) detonation velocity.¹⁶ The wave structure and relaxation process around the triple-point is of particular importance in affecting the ODW behavior.^{17,18,22} By altering the inflow Mach number (6.6–7.0), various flow configurations, such as λ -shaped, X-shaped, and Y-shaped shock structure, could be observed; moreover, the secondary ODW can convert to a normal detonation wave.²³ Cellular structure is an essential characteristic of normal detonations and plays a crucial role in affecting the stability of detonation propagation. For ODW, analogous cellular structures were also observed in numerical simulations.^{24–26} It was found that the resulting stability of the ODW front depends upon activation energy, wedge angle, and Mach number.^{27–29} The pattern of cellular structure is primarily determined by the left- and right-running transverse waves (TWs), which result from the periodic alteration of the reaction zone thickness due to the spatial or temporal oscillation of the leading shock front. The periodic perturbations of inflow,^{30,31} such as sinusoidal pressure and density disturbance, exhibit impacts on the initiation of ODW, cellular-like structure, and the motion of the triple-point on the ODW front. The Mach reflection of ODW impinging on an outward turning wall, owing to the post-surface thermal choking and the enhanced surface instability,³² the ODW front moves upstream movement and thus cannot be anchored on the wedge.³³

Nevertheless, the state-of-the-art numerical simulations have not fully unveiled the effects of viscosity on the initiation and evolution of ODWs. Rosato *et al.*¹³ showed that the ODW front undergoes a cycle-to-cycle variation of underdriven-to-overdriven detonation, which can be attributed to the flow turbulence. The existing studies^{34,35} demonstrated that the increasing temperature in the boundary layer (BL) of the induction region leads to an earlier onset of the overall ODW structure. Meanwhile, the presence of the BL strengthens the OSW and consequently facilitates the formation of ODW.³⁶ The OSW-to-ODW abrupt transition results from the upward motion of the triple-point with inflow parameters 1.0 atm, 300 K, and $Ma = 7.0$, which shall be attributed to shock/BL interaction.³⁷ Therefore, the Euler equation must be replaced by Navier–Stokes equation in the simulation in order to underline the mechanism for this enhancing effect of ODW formation. In turbulent flow, increasing turbulence intensity would switch abrupt transition to smooth transition and facilitates the initiation of ODW.³⁸ Considering the viscous effects enables the

resolution of the transverse wave/BL interaction, such as the appearance of separation bubble^{34,39} (see Fig. 1), which has been observed in the experimental study by Zhang *et al.*⁴⁰ During the evolution of wedge-induced ODW, two close separation bubbles may coalesce, the subsequent expansion of which tends to accelerate the ODW propagation downstream and eventually leads to flowing out of the wedge.⁴¹ The separation bubble evolution behavior caused by the ODW/BL interaction could play a crucial role in determining the combustion modes for real combustion facilitates. Under suitable conditions, a stabilized overdriven normal detonation wave might be produced.^{42,43} The existing studies manifested the importance of fluid viscosity during the evolution of ODW with emphasis on the shock-induced separation flows (such as OSW/BL and ODW/BL interaction) as well as its impact on the wave configuration. Nevertheless, the effects of viscosity on ODW initiation and the subsequent wave structures have not been fully understood, which motivates the current study.

In Sec. II, the Reynolds-averaged Navier–Stokes (RANS) equation incorporating the Spalart–Allmaras turbulence model and two-step chemical reaction is presented, and the numerical scheme and computation setup are introduced. In Sec. III, the initiation characteristics and effects of the burning BL for the wedge-induced ODW are studied with the dimensionless activation energy. The characteristic length and evolution of ODW initiation are analyzed under the viscous condition; a new wave structure emerges from the intersection of the burning BL and the CW, which affects the reflection pattern near the triple-point; and the long-term development of the burning BL contributes to the oscillation of the ODW flow field for large activation energy.

II. NUMERICAL METHOD AND COMPUTATION SETUP

A. Governing equations and discretization

In the study, the two-dimensional reactive Navier–Stokes equations coupled with a two-step chemical chain-branching kinetics model are employed. The nondimensional formulation in curvilinear coordinates is given as follows:⁴⁴

$$\frac{\bar{W}}{\partial t} + \frac{\bar{F}}{\partial \xi} + \frac{\bar{G}}{\partial \eta} = \frac{1}{Re_\infty} \left(\frac{\bar{F}_v}{\partial \xi} + \frac{\bar{G}_v}{\partial \eta} \right) + \bar{S}, \quad (1)$$

with

$$\begin{aligned} \bar{W} &= J^{-1}W, \quad \bar{F} = J^{-1}(\xi_x F + \xi_y G), \quad \bar{G} = J^{-1}(\eta_x F + \eta_y G), \\ \bar{F}_v &= J^{-1}(\xi_x F_v + \xi_y G_v), \quad \bar{G}_v = J^{-1}(\eta_x F_v + \eta_y G_v), \quad \bar{S} = J^{-1}S, \end{aligned} \quad (2)$$

where J^{-1} , ξ_x , ξ_y , η_x , η_y are the grid metrics for coordinate transformation from (x, y) to (ξ, η) . W is the conservative solution vector, F and G are the convective terms, F_v and G_v are the diffusive terms, and S is the reaction source term

$$\begin{aligned} W &= [\rho \quad \rho u \quad \rho v \quad \rho E \quad \rho \lambda_I \quad \rho \lambda_R]^T, \\ F &= [\rho u \quad \rho u^2 + p \quad \rho uv \quad (\rho E + p)u \quad \rho u \lambda_I \quad \rho u \lambda_R]^T, \\ G &= [\rho v \quad \rho uv \quad \rho v^2 + p \quad (\rho E + p)v \quad \rho v \lambda_I \quad \rho v \lambda_R]^T, \\ F_v &= \left[0 \quad \tau_{xx} \quad \tau_{xy} \quad u\tau_{xx} + v\tau_{xy} + k_{\text{eff}} \frac{\partial T}{\partial x} \quad \rho D_{\text{eff}} \frac{\partial \lambda_I}{\partial x} \quad \rho D_{\text{eff}} \frac{\partial \lambda_R}{\partial x} \right]^T, \\ G_v &= \left[0 \quad \tau_{yx} \quad \tau_{yy} \quad u\tau_{yx} + v\tau_{yy} + k_{\text{eff}} \frac{\partial T}{\partial y} \quad \rho D_{\text{eff}} \frac{\partial \lambda_I}{\partial y} \quad \rho D_{\text{eff}} \frac{\partial \lambda_R}{\partial y} \right]^T, \\ S &= [0 \quad 0 \quad 0 \quad 0 \quad \rho \omega_I \quad \rho \omega_R]^T, \end{aligned} \quad (3)$$

where ρ is density, u and v the x - and y -direction components of velocity, E the total energy per mass, and p the pressure, respectively. The equation of state is

$$p = (\gamma - 1)\rho \left[E - \frac{u^2 + v^2}{2} + \lambda_R Q \right], \quad (4)$$

where Q is the energy released from the chemical reaction by consuming unit mass.

Following our previous work,⁴⁵ a two-step chemical reaction model referring to hydrogen–air mixtures is used here. The induction and exothermic reaction zone are, respectively, characterized by individual progress variables, denoted by λ_I and λ_R (the subscripts I and R refer to the induction and exothermic reaction, respectively), which vary from 0 to 1 during the reaction period. The chemical reaction ratio, ω_I and ω_R , is defined as follows:⁴⁶

$$\begin{aligned} \omega_I &= -K_I H(\lambda_I) \exp\left(-\frac{E_a}{RT}\right), \\ \omega_R &= K_R [1 - H(\lambda_I)](1 - \lambda_R)^\nu, \\ H(\lambda_I) &= \begin{cases} 1, & 0 < \lambda_I \leq 1, \\ 0, & \lambda_I \leq 0, \end{cases} \end{aligned} \quad (5)$$

where E_a is the activation energy, ν the reaction order, typically being specified as 0.5, and K_I and K_R the pre-exponential factors controlling the induced and exothermic reaction, respectively. The Heaviside function $H(\lambda_I)$ turns off the progress of λ_I at the end of the induction zone.

Stresses (τ_{xx} , τ_{xy} , and τ_{yy}) can be written in the same form as those in laminar flow

$$\begin{aligned} \tau_{xx} &= \frac{2}{3}\mu_{\text{eff}} \left(2 \frac{\partial u}{\partial x} - \frac{\partial v}{\partial y} \right), \quad \tau_{yy} = \frac{2}{3}\mu_{\text{eff}} \left(2 \frac{\partial v}{\partial y} - \frac{\partial u}{\partial x} \right), \\ \tau_{xy} &= \tau_{yx} = \mu_{\text{eff}} \left(\frac{\partial u}{\partial y} + \frac{\partial v}{\partial x} \right). \end{aligned} \quad (6)$$

The effective transport properties, that is, viscosity μ_{eff} , thermal conductivity k_{eff} , and mass diffusivity D_{eff} , should be modified by including enhancement due to turbulence, that is,

$$\begin{aligned} \mu_{\text{eff}} &= \mu_l + \mu_t, \\ k_{\text{eff}} &= k_l + k_t, \quad k = \frac{\mu c_p}{Pr}, \\ D_{\text{eff}} &= D_l + D_t, \quad D = \frac{\mu}{\rho Sc}, \end{aligned} \quad (7)$$

where subscripts l and t indicate laminar and turbulence parameters. The laminar viscosity μ_l can be calculated based on Sutherland law. In turbulent flow, the effective viscosity should be determined based on the adopted turbulent model, that is, Spalart–Allmaras turbulence model⁴⁷ in the conservative form without a trip term in this work, which has been applied in the study on shock wave/BL interaction⁴⁸ and detonation engine^{41,49} and achieves comparable numerical results. With knowledge of viscosity, the remaining transport properties could be evaluated in terms of the nondimensional parameters, that is, the Prandtl number and Schmidt number. These parameters for laminar flow are specified to be $Pr = 0.72$ and $Sc = 0.5$, which are corrected to be $Pr = 0.9$ and $Sc = 0.5$ when the flow becomes turbulent.

All physical parameters in the governing equations are normalized by referring to the uniform free stream (the subscript ∞), such as $x = \frac{x^*}{l_{\text{ref}}}$, $u = \frac{u^*}{u_\infty}$, $p = \frac{p^*}{p_\infty}$, $T = \frac{T^*}{T_\infty}$, $Q = \frac{Q^*}{u_\infty^2}$, $\Psi = \frac{\Psi^*}{R_\infty c}$, where Ψ represents the specific gas constant or specific heat here.

The convective fluxes are calculated via the fifth-order weighted essentially non-oscillatory (WENO) finite difference method⁵⁰ combined with a Riemann problem solver and the Roe–HLLC method.^{51,52} To suppress numerical dissipation and improve the resolution efficiency of the origin WENO–JS scheme, the WENO–Z method is adopted here with the new smoothness indicators.⁵³ The discretization of viscous terms is processed by the fourth-order accuracy finite central differencing scheme in the least stencil restricted by the total width of the fifth-order WENO stencils with various Taylor expansion coefficients.^{54,55}

An ordinary differential equation is determined via spatial discretization, which can be solved through semi-implicit additive Runge–Kutta (ARK) methods. The ARK approach can effectively deal with the stiffness issue caused by chemical reactions. The open-source package ARKode, developed by Lawrence Livermore National Laboratory,⁵⁶ has been incorporated into our solver to fulfill the temporal discretization. The butcher table employed in the current ARK method is ARK4(3)6L [2]SA⁵⁷ and can achieve fourth-order accuracy in time-marching.

B. Physical model and flow condition

A schematic depiction of the computational domain is presented in the right part of Fig. 1. The angle of the wedge is fixed at $\theta_W = 25^\circ$. The free stream is parallel to the horizontal direction. The inlet boundary is supersonic uniform inflow, and the upper and outlet boundaries are zeroth-order extrapolation outflow. The surface of the wedge is subject to no-slip and adiabatic conditions.

Based on the classic physicochemical values of hydrogen–air mixtures,⁴⁶ the physical–chemical parameters of supersonic reactive flow are specified as $P_\infty = 1.0 \times 10^5$ Pa, $T_\infty = 300$ K, $Q^*/R_\infty T_\infty = 50$, $E_a = E_a^*/R_\infty T_\infty$, where E_a varies from 30 to 50, and the range

of E_a is also adopted by Zhang *et al.*⁵⁸ when considering the effects of initial pressure in simple chemical reaction model. Across the detonation structure, the initially unburnt mixture alters to the von Neumann states as passing through the shock wave and eventually converts to the burnt combustion products at the end of the reaction zone downstream. The variations of the mixture states are characterized by distinct heat capacity ratios.

Comprehensive examinations on the evolution of hydrodynamic discontinuities and the unsteadiness of detonation in turbulent flow are performed using the in-house solver, which has also been employed to determine the flow configurations and evolution of ODW in our previous study.^{45,49} The grid independence, monitoring the wall-distributed pressure and temperature, had been tested using a finite length wedge-induced ODW with inflow Mach number 7.0, wedge angle 29.0° , and the viscous computation proves that the grid size, $20.0 \mu\text{m}$ for the far-wall grid and $0.2 \mu\text{m}$ for the first layer grid of the wall, can resolve the flow configurations well,⁴⁹ and accordingly is utilized in the present study.

III. RESULTS AND DISCUSSION

The activation energy plays a crucial role in affecting the fundamental flow structures of wedge-induced ODW. The numerical simulations by parametrically varying the E_a are visualized in Fig. 2. The major wave configuration in the current viscous simulation is a triple-point connecting the OSW, CW, and ODW, which is analogous to the inviscid computation.^{18,23} The activation energy determines the sensitivity of the reaction rate to the flow temperature. As the nondimensional activation energy E_a increases from 30 to 50, the reaction rate is substantially suppressed; consequently, the ODW appears at a larger distance from the edge and meanwhile evolves over a longer period. It is also found that near the ODW triple-point, the regular reflection (RR) gradually transforms to the Mach reflection with rising E_a . Owing to the high temperature close to the wedge surface, the burning BL stretches from the wedge tip and joins the CW downstream. An in-depth discussion is given in Secs. III A and III B to interpret the effect of burning BL on initiation characteristics and wave configuration of wedge-induced ODW.

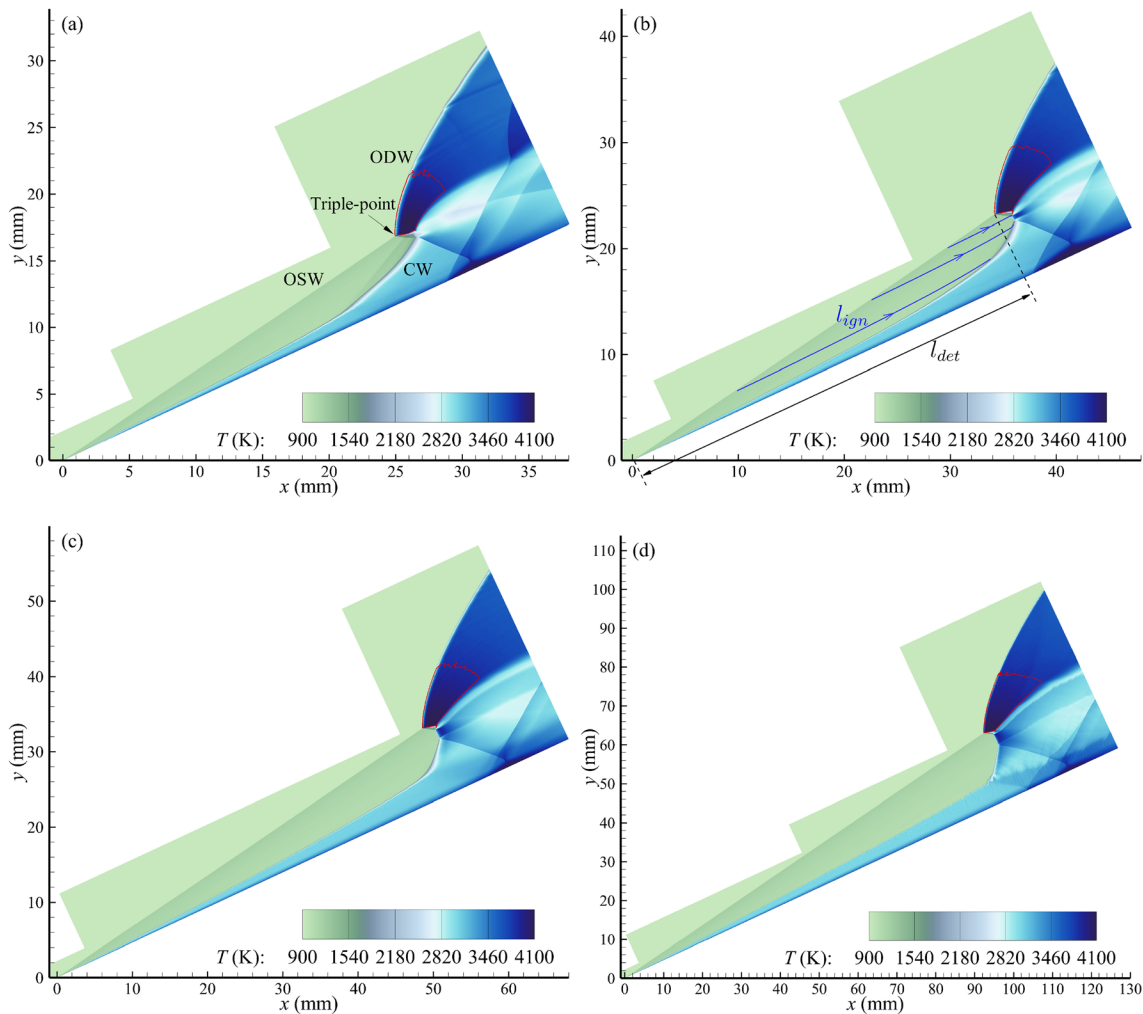


FIG. 2. Temperature contours of ODW with different activation energy: $E_a = 30$ (a), $E_a = 35$ (b), $E_a = 40$ (c), and $E_a = 50$ (d) (red solid line: sonic line).

A. Initiation of ODW

1. Induction ignition length

The induction ignition length l_{ign} is defined as the distance from the inert OSW to the following reaction front [see Fig. 2(b)] and can thus be determined by monitoring the reaction progress along the streamline crossing the post-shock flow field. It also can be theoretically calculated with OSW jump relation and chemical kinetic model via $l_{ign} = u_{OSW} \cdot t_{ind}$ for simplicity²⁵ (u_{OSW} is the post-OSW velocity and t_{ind} is the induction time that reactant behind OSW suffered), which is considered as the minimum length for wedge-triggered ODW.⁵⁹ For the partial OSW front near the wedge surface, l_{ign} curves are of similar geometry for all E_a , as shown in Fig. 3(a), which can be attributed to the high temperature in the BL, that is, approximately 10.8 times higher than the inflow temperature. In such high-temperature conditions, the induction reaction in association with heat release takes place readily instead of being dominated by shock-induced combustion. Outside the burning boundary layer, the temperature ratio induced by the OSW is around 3.6, that is, substantially smaller than that in the BL, and consequently, a positive correlation between the maximum l_{ign} and E_a can be inferred. With higher activation energies, for example, $E_a = 40$ and 50, a longer l_{ign} contributes to a sufficient development of the burning BL.

Figure 3(b) indicates good agreement between computation results and predicted values at relatively low activation energies, that is, $E_a \leq 35$. As E_a increases, the shock-induced combustion is delayed and the BL develops and thickens along the wedge surface. It causes the deflection angle of fluid particles passing through OSW larger than the wedge angle so that the wave angles of inert OSW are 0.9° – 1.9° higher than the predicted value (32.4°) based on the quasi-steady flow field. It suggests that the OSW tends to be intensified, which facilitates the chemical reaction with higher post-shock temperature and thus lowers the induction length l_{ign} compared with the predicted value for $E_a \geq 40$. Subsequent to the initiation of ODW, it arrives at the quasi-steady stage, during which an additional characteristic length l_{det} is defined as the distance from the wedge tip to the projection of the triple-point of ODW on the wedge surface [see Fig. 2(b)]. Obviously,

the l_{det} is more suitable to evaluate the minimal length for a successful wedge-induced ODW. For E_a ranging from 30 to 40, the l_{det} in both initiation and quasi-steady stages is greater than the predicted l_{ign} , implying that the ODW will not be established on an improper wedge if the forecasted l_{ign} is adopted as a guideline to estimate wedge length, and therefore, a redundancy length should be considered in the practical ODWE design.

2. Collision between combustion and shock

To clarify the role of shock-induced combustion during the initiation and evolution of ODW, the closed-up numerical Schlieren images of typical snapshots are given in Fig. 4. At $t = 18.88$ and 35.77 [see Figs. 4(a-i) and 4(b-i)], reactive fluid element passing through inert OSW is ignited at individual induction distances. The combustion products with smaller density and higher temperature tend to push the reactive wave from the wedge surface toward inert OSW. Two modes of reactive wave and shock wave interactions can be observed depending on the activation energy. With relatively low activation energy, that is, $E_a = 30$, the leading shock front and reaction front are decoupled, while with the relatively higher activation energy, that is, $E_a = 40$, the reactive is coupled. The reactive wave would unavoidably collide with the inert OSW, generating a local high-temperature region [see Figs. 4(a-ii) and 4(b-ii)] and triggering rapid chemical reaction. An outward movement of the reactive wave is driven by the high-temperature and high-pressure products. Consequently, a strong overdriven ODW (OODW) is established through the collisional interaction. Close to the triple point, the pressure of the OODW is 7.0 – 7.5 MPa [see Figs. 4(a-iii) and 4(b-iii)], which is much higher than the theoretical value (5.5 MPa) of the strong solution for ODW. As the OODW evolves, the subsonic zone behind the OODW broadens in association with gradual fall of pressure. Figure 5 shows the temporal variation of pressure close to the triple point of the OODW. It indicates that the pressure in the long-term limit tends to be independent of the activation energy and is approximately 5.8 MPa close to the maximum theoretical value of strong ODW. The initiation process of ODW can be deemed as the coupling

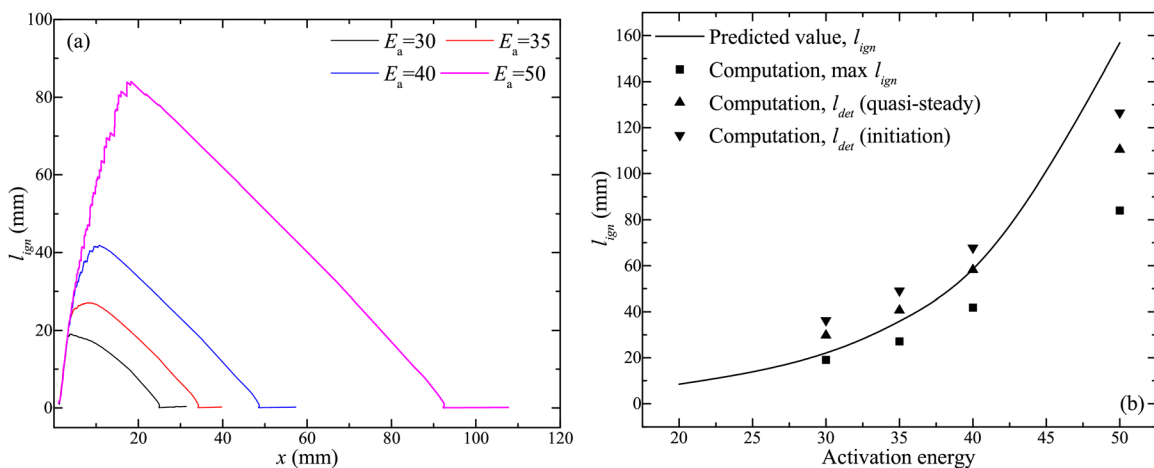


FIG. 3. Induction ignition length along the wave front of OSW/ODW (a) and comparison with the predicted values (b) with different activation energies.

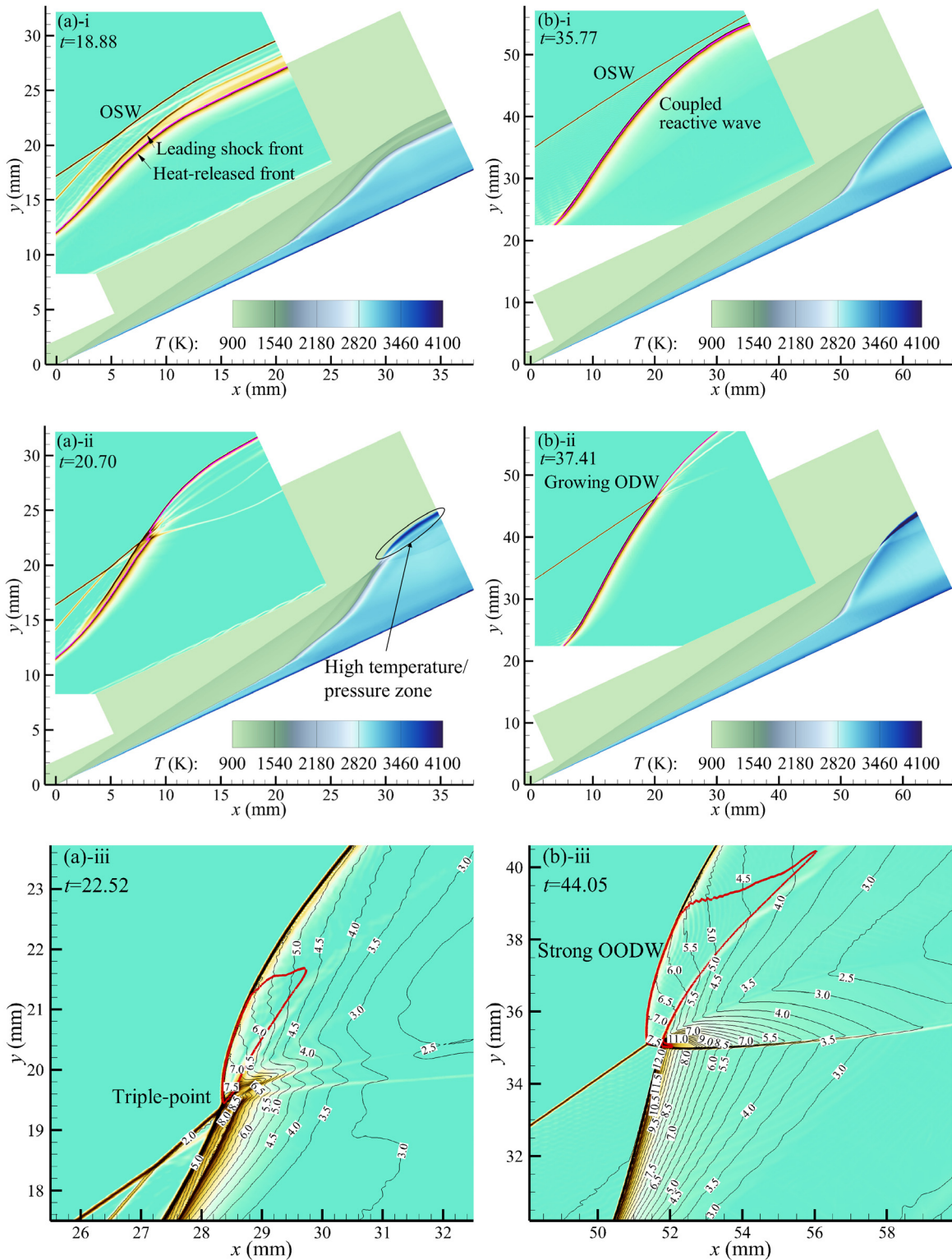


FIG. 4. Numerical Schlieren image near triple-point for typical snapshots of ODW initiation procedure when $E_a = 30$ (a) and 40 (b) (solid line: red-sonic line; purple-production mass fraction, $\lambda_R = 0.05$).

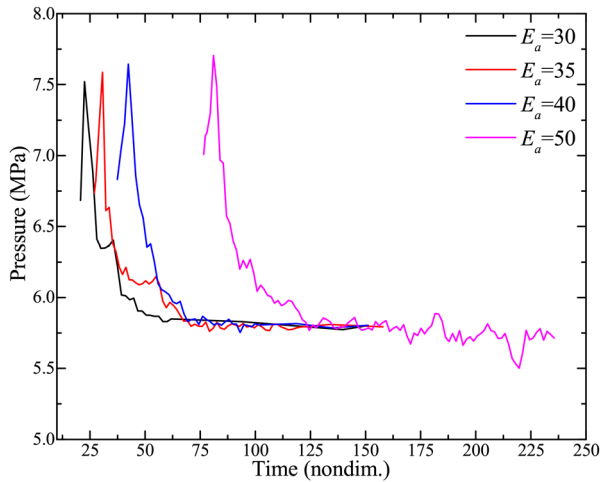


FIG. 5. Pressure evolution near triple-point behind strong OODW for various E_a .

effects of reactive wave diffraction and shock wave/reactive wave collision.

In particular, more attention should be paid to the subsonic zone behind strong OODW, where any acoustic disturbances can propagate upstream. The profile of the subsonic zone is enclosed by the sonic line, as shown in Fig. 2, and the area of the subsonic region is proportional to E_a , which increases from 9.95 to 112.47 mm². As activation energy increases, the shock front and heat-released front are highly coupled, which lead to a severe collision with inert OSW and induce a larger zone of strong OODW, and accordingly, the area of the subsonic region grows. However, an increment of E_a also leads to the chemical reaction rate slowing down, which tends to weaken the coupling between the leading shock front and the reaction front. Therefore, it is necessary to reveal the formation reason for stronger

CW during the formation of OODW, and the mechanism will be discussed in Sec. III B.

B. Effects of burning boundary layer

The impacts of BL on CW as well as the detonation evolution are discussed in-depth in this section, to clarify whether new wave configurations emerge with the existence of the burning BL. The pressure distribution of the wedge wall with $E_a = 30-50$ is shown in Fig. 6(a). Several stages of substantial pressure rise can be recognized, such as the separation and reattachment shock waves. Figure 6(b) presents the numerical Schlieren and iso-pressure contour, which indicates that a succession of pressure waves are emanated from the conjunction point of the burning BL and CW and subsequently reflects at the solid wall. With relatively high activation energy, for example, $E_a = 50$, a shock wave is formed [as shown in Fig. 8(b)], and a significant pressure jump across the reflection point (from 2.07 to 4.10 MPa) is observed, which can be attributed to the pressure accumulation near the conjunction point due to longer induction length. At intermediate activation energies, for example, $E_a = 35, 40$, the reflection point close to the separation bubble experiences a less remarkable step of pressure jump. However, at relatively low activation energy, for example, $E_a = 30$, the pressure increases from 1.97 to 2.76 MPa. Therefore, the pressure rise at the reflection point is proportional to the E_a .

1. Irregular reflection

The polar line analysis is used to grasp the transition principle between regular and irregular reflection for transverse wave/CW interaction near the ODW triple-point with emphasis on the effects of burning BL. The relationship between pressure ratio and deflection angle has been presented in our earlier study.⁴⁵ Because of the curvature effects and chemical reaction, it is difficult to completely describe the state at the post-front in terms of only one polar line. Instead, we will focus on a small region of the post-front to obtain a qualitative understanding of the interaction transition. Positive angles in the

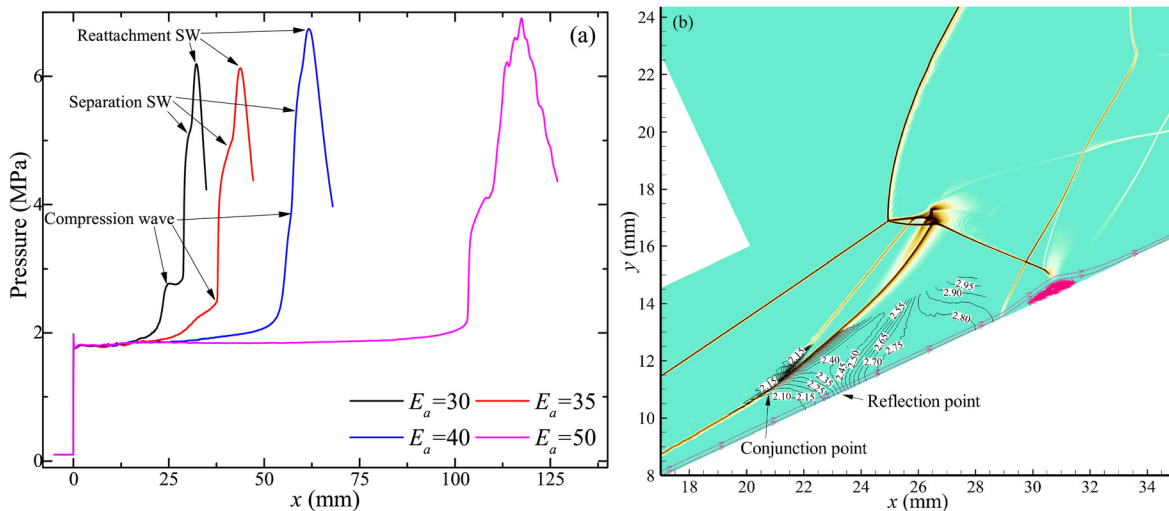


FIG. 6. Pressure profile along wedge surface (a) with various activation energy and local numerical Schlieren image (b) of ODW transition region when $E_a = 30$ (iso-pressure line: 2.0–3.0 MPa).

shock polar lines correspond to clockwise deflections in the following discussion.

The polar lines of TW, ODW, and CW are depicted in Fig. 7(a), where the intersection points of polar lines accordingly refer to the number labels indicated in Fig. 7(b). In the presence of BL, the effective deflection angle in region (1) is $0.8^\circ\text{--}1.6^\circ$ larger than the wedge angle over the considered activation energy range, that is, $E_a = 30 - 50$. In spite of discrepancies in the OSW strength at different E_a , the parameters characterizing the post-shock state do not vary significantly. Approximately, the post-OSW state could be specified at point (1) with a wedge angle of 25° on polar line R_{OSW} . The crossing point (2) between R_{ODW} and the polar line (for the TW) originating from point (1) characterizes the state behind ODW, which locates at the strong solution branch. Providing that the leading shock of the overdriven ODW is sufficiently strong, the local post-ODW state appears to be insensitive to the activation energy. It indicates that the pressure ratio in region (2) takes the numerical value of about 58 for all E_a (see Fig. 5), which is in good agreement with 55 from polar diagrams. Accordingly, in our simulation with $E_a = 30 - 50$, the state behind strong overdriven ODW could be represented by point (2). The possible states across CW are located on polar line R_1 originating from point (1). The polar line R_2 describes the states behind reactive waves with the coming flow condition represented by point (2). The curves R_1 and R_2 intersect at the point (5m), which locates at the left strong solution branch of R_1 and accordingly implies the occurrence of an inverse Mach reflection (InMR).

The state behind CW plays a decisive role in determining the reflection type of TW/CW interaction. Figure 7(b) shows that the wave angle along the curved CW would continue to increase rather than remain constant. Along the CW, we can define two typical zones (3) and (7), which is marked in Fig. 7(b). Due to the existence of pressure wave or shock wave near the conjunction point of burning BL and CW, pressure in region (7) is greater than that in region (6), and their difference becomes higher as E_a increases. To match the high-pressure zone, the deflection angle of CW for region (7) must raise, and so does that for region (3). As shown in Fig. 7(a), points

(3), (3'), and (3'') corresponding to deflection angles 8° , 24° , and 28° , respectively, are utilized to describe the typical state behind the CW at selected E_a . Then, point (4) can be determined via overlap condition between R_3 (or R'_3, R''_3) and R_2 (or R_1), where $R_3, R'_3,$ and R''_3 are polar lines originating from points (3), (3'), and (3''), respectively.

When the deflection angle of CW (θ_{comb}) is relatively small (8°), the overlap point between polar lines R_3 and R_2 , denoted by point (4r), (5), locates at the weak solution branch, which theoretically implies the occurrence of a RR. Meanwhile, R_3 and R_2 intersect with the strong solution branch of R_1 at point (4m) and (5m), respectively. It suggests the Mach reflection (MR), and a divergent stream tube will be formed behind the Mach stem (MS). In the absence of unique boundary condition downstream, the subsonic flow cannot be accelerated to match the supersonic flow downstream, which results in the prohibition of MR. Thus, for $\theta_{comb} = 8^\circ$, only RR is admissible. As the deflection angle of CW increases, for example, $\theta_{comb} = 24^\circ$, the intersection of the weak solution branches of R'_3 and R_2 at point (4'r), (5) can still be seen, which remains the possibility of RR. However, the deflection angle of the crossing point (4'm) determined by R'_3 and R_1 alters. Specifically, the direct Mach reflection (DiMR) occurs, which is associated with a Mach stem consisting of DiMR and InMR, and it leads to a convergence stream tube and thus matches the supersonic flow downstream. Therefore, the situation characterized by $\theta_{comb} = 24^\circ$ is in the dual-solution region, in which both RR and MR are available. The critical condition for the transition from RR to dual-solution region can be determined by the single point where $R'_3, R_2,$ and R_1 intersect simultaneously. According to the polar line analysis, the critical deflection angle is evaluated to be $\theta_{comb} = 22.6^\circ$. For $\theta_{comb} = 28^\circ$, R''_3 and R_2 interact with the strong solution branch of R_1 at point (4'') and (5m), respectively. Nevertheless, there is no overlap between R''_3 and R_2 , and accordingly, only MR is admissible. Particularly, the critical condition for the transition from dual-solution region to single MR region can be determined when R_2 is tangential to the detachment point of R''_3 .

The deflection angles of CW corresponding to the activation energies 30, 35, 40, and 50 are $10^\circ, 21^\circ, 28^\circ,$ and 30° . Accordingly, an

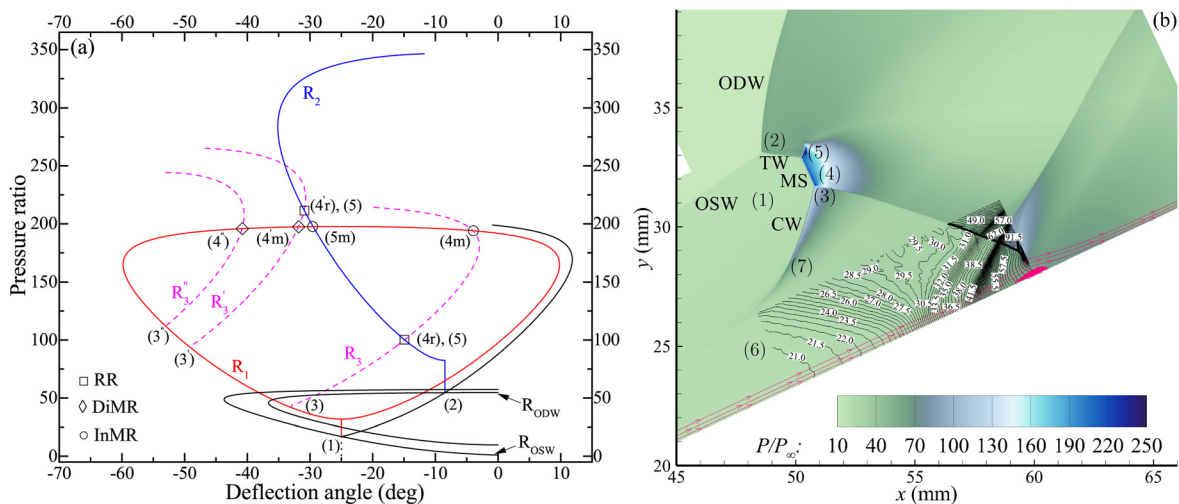


FIG. 7. Polar line of shock reflection (a) and closed-up pressure contours (b) for ODW transition zone with Mach reflection ($E_a = 40$).

MR is observed for $\theta_{\text{comb}} \geq 21^\circ$, which is slightly less than the lower critical value (22.6°) for the dual-solution zone via polar line analysis. The effect of chemical reaction may facilitate the MR when E_a increases.

2. Oscillation of wave structure

In addition to the effects of the burning BL on the wave configuration of ODW, the Rayleigh–Taylor (R–T) instability is provoked by the favorable density gradient at the downstream BL. To analyze the steadiness of the ODW flow, the impacts of the R–T instability must be accessed. Then, during a typical period, the Cartesian coordinates of the triple-point of ODW and bottom end point of Mach stem [see P1 and P2 in Fig. 8(b)] are extracted and transformed to polar coordinates (r, θ) , and r is replaced with $\bar{r} = r - r_{\text{min}}$ (r_{min} is the minimal value of polar coordinate r). The (\bar{r}, θ) vs time is illustrated with the style of the bubble diagram in Fig. 8(a), where the vertical coordinate is the polar angle θ and the area of bubbles is characterized by \bar{r} . The polar angle of the ODW triple-point in the period is stable, hovering

around 34.3° , which compares well with the wave angle of inert OSW; the \bar{r} suffers a diminishment following by a raise, which manifests that the ODW triple-point moves forward and backward along the inert OSW with a small oscillation amplitude. For the bottom end point of the Mach stem (P2), both \bar{r} and θ exhibit a clear variation [see Fig. 8(a)], which undergoes a more severe fluctuation than the ODW triple-point. Especially, the dimensionless time here is nearly in the magnitude of $10^0 \mu\text{s}$, and the oscillation recorded in the current simulation can be considered as high frequency.

The activation energy characterizes the sensitivity of the reaction rate to temperature variation, which can be triggered by the propagation of pressure waves in the burning BL. The reaction enhancement due to such temperature perturbation could be stronger in the burning BL for larger activation energy, which can evoke flow perturbation. As the burning BL develops for wedge-induced ODW ($E_a = 50$), the relatively smooth flame surface near the wedge tip tends to become corrugated. Because of the long-distance/long-time growth of the burning BL, the bubbles composed of low-density combustion products accelerate into the high-density reactants behind inert OSW, which initiates

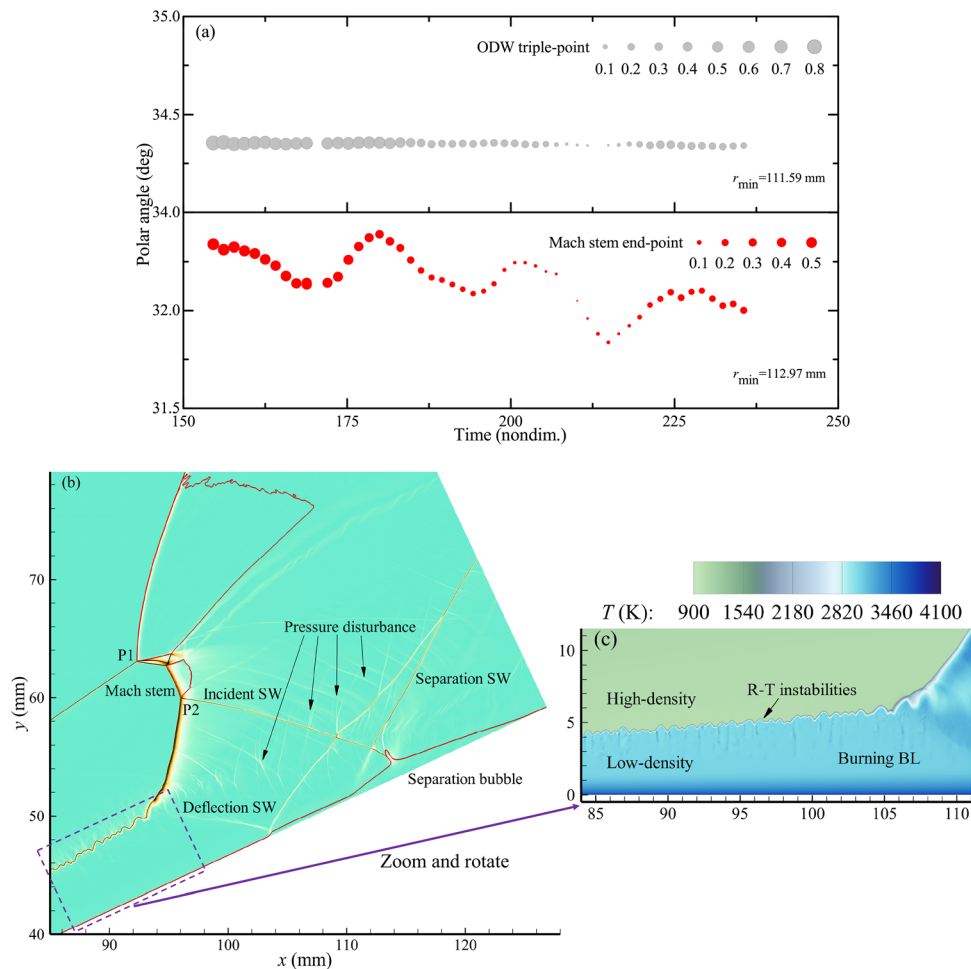


FIG. 8. Change trend of the triple-point (a), zoomed-in numerical Schlieren image (b), and temperature contour (c) of ODW when $E_a = 50$.

the R–T instabilities as indicated in Fig. 8(b). The bubble and spike structures grow periodically and alternately, leading to the oscillation of the CW in association with the BL. The fluctuating CW interacts with the transverse wave causing Mach reflection and thus transmits the oscillating behavior to both Mach stem and incident shock wave (SW). The unsteady incident SW impinges on the wall, leading to the establishment of the separation bubble. The unstable incident SW aggravates the self-excited oscillation of the separation bubble, which propagates upstream through the subsonic region of the BL, acting as an input excitation for the point of deflection SW impinging on the wall. Thus, the deflection SW moves in a reciprocating motion along the wedge wall, which feeds back to the conjunction point of CW and the burning layer. Meanwhile, the pressure disturbance caused by the CW and burning BL propagates downward, acting as the excitation factor for the wave structure downstream.

IV. CONCLUSIONS

In this work, we have conducted a high-resolution simulation to describe the initiation and evolution of the wedge-induced oblique detonation wave (ODW) with emphasis on the effects of the burning boundary layer (BL). The Reynolds-averaged Navier–Stokes equation equipped with Spalart–Allmaras turbulence model and a two-step chemical reaction has been numerically solved using WENO-Z reconstruction and the additive Runge–Kutta method.

The induction ignition length l_{ign} behind OSW/ODW front shows a maximum value, which is proportional to activation energy (E_a), and effectively governed by the burning BL near the wedge surface, but by the shock-induced combustion outside the burning BL. During the initiation of ODW, the collision occurs between the shock-induced combustion wave and the inert OSW, which forms a high-pressure/temperature zone expanding outwards, known as the diffraction of the reactive wave. The area of the subsonic zone behind strong overdriven ODW monotonically increases with the intensity of combustion wave in the quasi-steady flow field.

A series of compression waves (or shock wave) are emanated from the conjunction point of the burning BL and combustion wave, which further strengthens the pressure jump as E_a increases. In the presence of those compression waves, the deflection angle of the combustion wave becomes larger to match the resulting high-pressure zone. According to the polar line analysis, regular reflection transitions into irregular reflection as the deflection angle becomes larger, which agrees well with the numerical simulation. Particularly, for $E_a = 50$, the reaction front of the burning BL is subject to Rayleigh–Taylor instabilities, which leads to oscillations of the triple-point and Mach stem of the ODW flow structure.

The current work shows that the burning BL contributes to the ODW initiation and reflection type near triple-point. To avoid the oscillation of the flow configuration and thus to hold the ODW steady, the development of the burning BL should be suppressed appropriately, and the induction ignition length must be precisely controlled via the hot jet mounted on the wall or a novel geometry configuration. In addition, the simulation results demonstrate that the strength of the compression wave emanated from the conjunction point of the burning BL and the combustion wave depends on the activation energy. However, there is no quantitative prediction in theory. To address this issue in the future, an elaborate theoretical model based on boundary layer theory, chemical kinetics, and shock relation should be

developed, which can also assess the strength of the combustion wave; with the aid of shock/combustion interaction, a fundamental profile on the ODW flow field can be established theoretically while accounting for the effects of BL.

ACKNOWLEDGMENTS

The research is supported by the National Natural Science Foundation of China (Nos. U2141220, 11672309, and 52006001), and the Youth Project of Science and Technology Research Program of Chongqing Education Commission of China (No. KJQN202200739).

AUTHOR DECLARATIONS

Conflict of Interest

The authors have no conflicts to disclose.

Author Contributions

Li Yang: Conceptualization (equal); Formal analysis (lead); Software (lead); Writing – original draft (lead); Writing – review & editing (supporting). **Lianjie Yue:** Conceptualization (lead); Funding acquisition (lead); Supervision (lead). **Dehai Yu:** Funding acquisition (equal); Writing – review & editing (lead). **Zheng Chen:** Writing – review & editing (equal).

DATA AVAILABILITY

The data that support the findings of this study are available from the corresponding author upon reasonable request.

REFERENCES

- 1P. Wolański, “Detonative propulsion,” *Proc. Combust. Inst.* **34**, 125–158 (2013).
- 2K. Wu, S. J. Zhang, D. W. She, and J. P. Wang, “Analysis of flow-field characteristics and pressure gain in air-breathing rotating detonation combustor,” *Phys. Fluids* **33**, 126112 (2021).
- 3K. Kailasanath, “Review of propulsion applications of detonation waves,” *AIAA J.* **38**, 1698–1708 (2000).
- 4J. Urzay, “Supersonic combustion in air-breathing propulsion systems for hypersonic flight,” *Annu. Rev. Fluid Mech.* **50**, 593–627 (2018).
- 5Q. Liu, D. Baccarella, and T. Lee, “Review of combustion stabilization for hypersonic airbreathing propulsion,” *Prog. Aerosp. Sci.* **119**, 100636 (2020).
- 6R. Dubeout, J. P. Sisljan, and R. Oppitz, “Numerical simulation of hypersonic shock-induced combustion ramjets,” *J. Propul. Power* **14**, 869–879 (1998).
- 7J. Chan, J. P. Sisljan, and D. Alexander, “Numerically Simulated Comparative Performance of a Scramjet and Shcramjet at Mach 11,” *J. Propul. Power* **26**, 1125–1134 (2010).
- 8Z. Jiang, Z. Zhang, Y. Liu, C. Wang, and C. Luo, “Criteria for hypersonic air-breathing propulsion and its experimental verification,” *Chin. J. Aeronaut.* **34**, 94–104 (2021).
- 9C. Viguier, L. F. F. d Silva, D. Desbordes, B. Deshaies, L. F. F. d Silva, D. Desbordes, and B. Deshaies, “Onset of oblique detonation waves: Comparison between experimental and numerical results for hydrogen-air mixtures,” *Symp. (Int.) Combust.* **26**, 3023–3031 (1996).
- 10H. F. Lehr, “Experiments on shock-induced combustion,” *Astronaut. Acta* **17**, 589–597 (1972).
- 11J. Liu, J. Liou, M. Sichel, C. Kauffman, and J. Nicholls, “Diffraction and transmission of a detonation into a bounding explosive layer,” *Symp. (Int.) Combust.* **21**, 1639–1647 (1988).
- 12E. K. Dabora, D. Desbordes, and C. Gueraudj, “Oblique detonation at hypersonic velocities,” in *Dynamics of Detonations and Explosions: Detonations*,

- edited by A. A. Borisov, A. L. Kuhl, J.-C. Leyer, and W. A. Sirignano (Progress in Astronautics and Aeronautics, Washington, 1991), pp. 187–201.
- ¹³D. A. Rosato, M. Thornton, J. Sosa, C. Bachman, G. B. Goodwin, and K. A. Ahmed, “Stabilized detonation for hypersonic propulsion,” *Proc. Natl. Acad. Sci. U. S. A.* **118**, e2102244118 (2021).
 - ¹⁴C. Li, K. Kailasanath, and E. S. Oran, “Detonation structures behind oblique shocks,” *Phys. Fluids* **6**, 1600 (1994).
 - ¹⁵L. F. Figueria Da Silva and B. Deshaies, “Stabilization of an oblique detonation wave by a wedge: A parametric numerical study,” *Combust. Flame* **121**, 152–166 (2000).
 - ¹⁶S. Miao, J. Zhou, S. Liu, and X. Cai, “Formation mechanisms and characteristics of transition patterns in oblique detonations,” *Acta Astronaut.* **142**, 121–129 (2018).
 - ¹⁷H. Teng, Y. Zhang, and Z. Jiang, “Numerical investigation on the induction zone structure of the oblique detonation waves,” *Comput. Fluids* **95**, 127–131 (2014).
 - ¹⁸Y. S. Liu, Y. S. Liu, D. Wu, and J. P. Wang, “Structure of an oblique detonation wave induced by a wedge,” *Shock Waves* **26**, 161–168 (2016).
 - ¹⁹G. X. Xiang, X. Gao, W. J. Tang, X. Z. Jie, and X. Huang, “Numerical study on transition structures of oblique detonations with expansion wave from finite-length cowl,” *Phys. Fluids* **32**, 056108 (2020).
 - ²⁰P. Yang, H. Teng, Z. Jiang, and H. D. Ng, “Effects of inflow Mach number on oblique detonation initiation with a two-step induction-reaction kinetic model,” *Combust. Flame* **193**, 246–256 (2018).
 - ²¹Y. Fang, Y. Zhang, X. Deng, and H. Teng, “Structure of wedge-induced oblique detonation in acetylene-oxygen-argon mixtures,” *Phys. Fluids* **31**, 026108 (2019).
 - ²²H. Teng, H. D. Ng, P. Yang, and K. Wang, “Near-field relaxation subsequent to the onset of oblique detonations with a two-step kinetic model,” *Phys. Fluids* **33**, 096106 (2021).
 - ²³H. Teng, C. Tian, Y. Zhang, L. Zhou, and H. D. Ng, “Morphology of oblique detonation waves in a stoichiometric hydrogen-air mixture,” *J. Fluid Mech.* **913**, A1 (2021).
 - ²⁴J.-Y. Choi, D.-W. Kim, I.-S. Jeung, F. Ma, and V. Yang, “Cell-like structure of unstable oblique detonation wave from high-resolution numerical simulation,” *Proc. Combust. Inst.* **31**, 2473–2480 (2007).
 - ²⁵P. Yang, H. Li, Z. Chen, C. Wang, and H. Teng, “Numerical investigation on movement of triple points on oblique detonation surfaces,” *Phys. Fluids* **34**, 066113 (2022).
 - ²⁶Z. Luan, Y. Huang, R. Deiterding, and Y. You, “On the evolutions of triple point structure in wedge-stabilized oblique detonations,” *Phys. Fluids* **34**, 067118 (2022).
 - ²⁷J. Verreault, A. J. Higgins, and R. A. Stowe, “Formation of transverse waves in oblique detonations,” *Proc. Combust. Inst.* **34**, 1913–1920 (2013).
 - ²⁸H. Teng, H. D. Ng, K. Li, C. Luo, and Z. Jiang, “Evolution of cellular structures on oblique detonation surfaces,” *Combust. Flame* **162**, 470–477 (2015).
 - ²⁹P. Yang, H. Teng, H. D. Ng, and Z. Jiang, “A numerical study on the instability of oblique detonation waves with a two-step induction-reaction kinetic model,” *Proc. Combust. Inst.* **37**, 3537–3544 (2019).
 - ³⁰Z. Ren, B. Wang, and L. Zheng, “Wedge-induced oblique detonation waves in supersonic kerosene-air premixing flows with oscillating pressure,” *Aerosp. Sci. Technol.* **110**, 106472 (2021).
 - ³¹P. Yang, H. D. Ng, and H. Teng, “Unsteady dynamics of wedge-induced oblique detonations under periodic inflows,” *Phys. Fluids* **33**, 016107 (2021).
 - ³²K. Wang, H. Teng, P. Yang, and H. D. Ng, “Numerical investigation of flow structures resulting from the interaction between an oblique detonation wave and an upper expansion corner,” *J. Fluid Mech.* **903**, A28 (2020).
 - ³³K. Wang, Z. Zhang, P. Yang, and H. Teng, “Numerical study on reflection of an oblique detonation wave on an outward turning wall,” *Phys. Fluids* **32**, 046101 (2020).
 - ³⁴J.-Y. Choi and I.-S. Jeung, “Numerical simulation of super-detonative ram accelerator: Its shock-induced combustion and oblique detonation,” in *Hypervelocity Launchers. Shock Wave Science and Technology Reference Library*, edited by F. Seiler and O. Igra (Springer, 2016), Vol. 10, pp. 217–267.
 - ³⁵C. Li, K. Kailasanath, and E. Oran, “Effects of boundary layers on oblique-detonation structures,” in *31st Aerospace Sciences Meeting* (American Institute of Aeronautics and Astronautics, Reston, VA, 1993).
 - ³⁶C. L. Bachman and G. B. Goodwin, “Ignition criteria and the effect of boundary layers on wedge-stabilized oblique detonation waves,” *Combust. Flame* **223**, 271–283 (2021).
 - ³⁷Y. Fang, Z. Zhang, and Z. Hu, “Effects of boundary layer on wedge-induced oblique detonation structures in hydrogen-air mixtures,” *Int. J. Hydrogen Energy* **44**, 23429–23435 (2019).
 - ³⁸M. Yu and S. Miao, “Initiation characteristics of wedge-induced oblique detonation waves in turbulence flows,” *Acta Astronaut.* **147**, 195–204 (2018).
 - ³⁹J.-Y. Choi, I.-S. Jeung, and Y. Yoon, “Scaling effect of the combustion induced by shock-wave boundary-layer interaction in premixed gas,” *Symp. (Int.) Combust.* **27**, 2181–2188 (1998).
 - ⁴⁰Z. Zhang, C. Wen, C. Yuan, Y. Liu, G. Han, C. Wang, and Z. Jiang, “An experimental study of formation of stabilized oblique detonation waves in a combustor,” *Combust. Flame* **237**, 111868 (2022).
 - ⁴¹S. Miao, D. Xu, T. Song, and J. Yu, “Shock wave-boundary layer interactions in wedge-induced oblique detonations,” *Combust. Sci. Technol.* **192**, 2345–2370 (2020).
 - ⁴²Z. Zhang, K. Ma, W. Zhang, X. Han, Y. Liu, and Z. Jiang, “Numerical investigation of a Mach 9 oblique detonation engine with fuel pre-injection,” *Aerosp. Sci. Technol.* **105**, 106054 (2020).
 - ⁴³Z. Zhang, C. Wen, W. Zhang, Y. Liu, and Z. Jiang, “Formation of stabilized oblique detonation waves in a combustor,” *Combust. Flame* **223**, 423–436 (2021).
 - ⁴⁴J. Blazek, *Computational Fluid Dynamics: Principles and Applications*, 3rd ed. (Butterworth-Heinemann, Oxford, 2015), p. 466.
 - ⁴⁵L. Yang, L. Yue, Q. Zhang, and X. Zhang, “Numerical study on the shock/combustion interaction of oblique detonation waves,” *Aerosp. Sci. Technol.* **104**, 105938 (2020).
 - ⁴⁶C. Leung, M. I. Radulescu, and G. J. Sharpe, “Characteristics analysis of the one-dimensional pulsating dynamics of chain-branching detonations,” *Phys. Fluids* **22**, 126101 (2010).
 - ⁴⁷S. R. Allmaras, F. T. Johnson, and P. R. Spalart, “Modifications and clarifications for the implementation of the Spalart-Allmaras turbulence model,” in 7th International Conference on Computational Fluid Dynamics, Hawaii, Big Island, 2012.
 - ⁴⁸F.-Y. Zuo, A. Memmolo, and S. Pirozzoli, “Reynolds-averaged numerical simulations of conical shock-wave/boundary-layer interactions,” *AIAA J.* **59**, 1645–1659 (2021).
 - ⁴⁹L. Yang, L. Yue, and Q. Zhang, “Onset of oblique detonation waves for a cavity-based wedge,” *AIAA J.* **60**, 2836–2849 (2022).
 - ⁵⁰G. S. Jiang and C. W. Shu, “Efficient implementation of weighted ENO schemes,” *J. Comput. Phys.* **126**, 202–228 (1996).
 - ⁵¹P. L. Roe, “Approximate Riemann solvers, parameter vectors, and difference schemes,” *J. Comput. Phys.* **135**, 250–258 (1997).
 - ⁵²B. Einfeld, “On Godunov-type methods for gas dynamics,” *SIAM J. Numer. Anal.* **25**, 294–318 (1988).
 - ⁵³F. Acker, R. R. Borges, and B. Costa, “An improved WENO-Z scheme,” *J. Comput. Phys.* **313**, 726–753 (2016).
 - ⁵⁴Y. Shen, B. Wang, and G. Zha, “Implicit WENO scheme and high order viscous formulas for compressible flows,” in *25th AIAA Applied Aerodynamics Conference* (American Institute of Aeronautics and Astronautics, Miami, FL, 2007), pp. 1756–1773.
 - ⁵⁵Z.-S. Sun, Y.-X. Ren, S.-Y. Zhang, and Y.-C. Yang, “High-resolution finite difference schemes using curvilinear coordinate grids for DNS of compressible turbulent flow over wavy walls,” *Comput. Fluids* **45**, 84–91 (2011).
 - ⁵⁶A. C. Hindmarsh, P. N. Brown, K. E. Grant, S. L. Lee, R. Serban, D. E. Shumaker, and C. S. Woodward, “SUNDIALS: Suite of nonlinear and differential/algebraic equation solvers,” *ACM Trans. Math. Software* **31**, 363–396 (2005).
 - ⁵⁷C. A. Kennedy and M. H. Carpenter, “Additive Runge-Kutta schemes for convection-diffusion-reaction equations,” *Appl. Numer. Math.* **44**, 139–181 (2003).
 - ⁵⁸Y. Zhang, L. Zhou, J. Gong, H. D. Ng, and H. Teng, “Effects of activation energy on the instability of oblique detonation surfaces with a one-step chemistry model,” *Phys. Fluids* **30**, 106110 (2018).
 - ⁵⁹G. Q. Zhang, S. F. Gao, and G. X. Xiang, “Study on initiation mode of oblique detonation induced by a finite wedge,” *Phys. Fluids* **33**, 016102 (2021).